Renewable Energy 69 (2014) 134–146

Contents lists available at ScienceDirect

Renewable Energy

journal homepage: www.elsevier.com/locate/renene

Phase change material with graphite foam for applications in high-temperature latent heat storage systems of concentrated solar power plants

Weihuan Zhao [a], David M. France [b], Wenhua Yu [a], Taeil Kim [a], Dileep Singh [c,*]

[a] Energy Systems Division, Argonne National Laboratory, 9700 South Cass Avenue, Argonne, IL 60439, USA
[b] Department of Mechanical and Industrial Engineering, University of Illinois at Chicago, 842 West Taylor Street (m/c 251), Chicago, IL 60607, USA
[c] Nuclear Engineering Division, Argonne National Laboratory, 9700 South Cass Avenue, Argonne, IL 60439, USA

ARTICLE INFO

Article history:
Received 1 November 2013
Accepted 12 March 2014
Available online

Keywords:
Concentrated solar power
Graphite foam–$MgCl_2$ combination
Latent heat thermal energy storage
Three-dimensional heat transfer simulation
Exergy efficiency

ABSTRACT

A high-temperature latent heat thermal energy storage (LHTES) system was analyzed for applications to concentrated solar power (CSP) plants (utilizing steam at ~610 °C) for large-scale electricity generation. Magnesium chloride was selected as the phase change material (PCM) for the latent heat storage because of its high melting point (714 °C). Because the thermal conductivities of most salt materials are very low, usually less than 1 W/m K, graphite foam was applied as an additive to considerably enhance the overall thermal conductivity of the resulting graphite foam–PCM combination in the LHTES system. The heat transfer performance and the exergy efficiency in the graphite foam–$MgCl_2$ LHTES system were considered for the design and optimization of the storage system. Three-dimensional (3-D) heat transfer simulations were conducted for the storage system using commercial software COMSOL. Three groups of analyses were performed for an LHTES system: using PCM alone without graphite foam, using average material properties for graphite foam–PCM combination, and using anisotropic thermal conductivity and temperature-dependent material properties for graphite foam–PCM. Results presented show that the graphite foam can help to significantly improve the heat transfer performance as well as the exergy efficiency in the LHTES system. They also show the effects of the anisotropic thermal conductivity and indicate capital cost savings for a CSP electric power plant by reducing the number of heat transfer fluid (HTF) pipes in the LHTES tank by a factor of eight.

1. Introduction

Thermal energy storage (TES) systems have been proposed for applications to CSP plants to store solar thermal energy in the daytime for usage when the sun is down in order to improve the plant capacity. Two general approaches have been applied to TES: sensible heat storage and latent heat storage. Existing CSP plants in the world use sensible heat storage systems for medium operation temperatures (less than 600 °C). For instance, Gemasolar in Seville, Spain uses the central tower technology and a molten salt, sensible heat storage system for solar power generation [1,2]. A two-tank direct system with liquid-state salts (60 mol% $NaNO_3$ + 40 mol% kNO_3) is used for the sensible heat storage. The plant capacity is 17 MWe with 15-h storage capacity [1,2]. Another example is Extresol-1 in Badajoz, Spain [1,3]. It also uses a two-tank, molten salt, sensible heat storage system. It has applied the parabolic trough technology and an indirect storage system [1,3], which requires an extra heat exchanger and pumps in the storage cycle. The plant capacity is 50 MWe with 7.5-h storage capacity [1,3]. Due to the large size and high cost of sensible heat storage systems, LHTES systems have been proposed for future CSP plants.

Latent heat storage using PCMs is a very promising method to store solar thermal energy. It can store thermal energy at a much higher density based on the latent heat of the material with a smaller volume requirement of the material and a smaller temperature difference. It can reduce the two-tank sensible storage system to a one-tank system decreasing the size and the cost of the storage system and thus simplifying it. Furthermore, latent heat storage can improve the thermal performance of the storage system partially through higher temperature. Fig. 1 is the conceptual energy flow scheme in CSP with LHTES system. In order to achieve

* Corresponding author. Tel.: +1 630 252 5009; fax: +1 630 252 5568.
E-mail address: dsingh@anl.gov (D. Singh).

http://dx.doi.org/10.1016/j.renene.2014.03.031
0960-1481/

Nomenclature

A	cross section area of heat transfer fluid pipe (m^2)
$B(T)$	liquid fraction
c_p	heat capacity (J/kg K)
D	inner diameter of heat transfer fluid pipes (m)
Ex	exergy (J)
h	heat transfer coefficient (W/m^2 K)
k	thermal conductivity (W/m K)
L	latent heat of fusion (J/kg)
M	mass of the graphite foam–PCM combination in the LHTES system (kg)
n	exponent
Pr	Prandtl number
r	radius (m)
Re_D	Reynolds number in heat transfer fluid pipes
T	temperature (K)
T_a	environment temperature (K)
T_m	melting point (K)
$T_{PCM,char}$	final temperature of graphite foam–PCM after charging process (K)
$T_{PCM,dis}$	final temperature of graphite foam–PCM after discharging process (K)
$T_{PCM,init}$	initial temperature of graphite foam–PCM (K)
t	time (s)
V	heat transfer fluid velocity (m/s)
$d\alpha/dT$	Gaussian function

Greek symbols

μ	dynamic viscosity (N s/m^2)
μ_s	dynamic viscosity at the wall (N s/m^2)
ρ	density (kg/m^3)
ψ	exergy efficiency (%)
$\psi_{overall}$	overall exergy efficiency (%)
ψ_{round}	round trip exergy efficiency (%)

Subscripts

char	charging process
combination_x	graphite foam–PCM combination in the x-direction
combination_y	graphite foam–PCM combination in the y-direction
combination_z	graphite foam–PCM combination in the z-direction
dis	discharging process
HTF	heat transfer fluid
HTF_char	heat transfer fluid during charging process
HTF_char_inlet	inlet heat transfer fluid during charging process
HTF_char_outlet	outlet heat transfer fluid during charging process
HTF_dis	heat transfer fluid during discharging process
HTF_dis_inlet	inlet heat transfer fluid during discharging process
HTF_dis_outlet	outlet heat transfer fluid during discharging process
l	liquid state
s	solid state

Acronyms

CSP	concentrated solar power
DSC	differential scanning calorimetry
FLiNaK	LiF–NaF–KF (46.5–11.5–42 mol%)
HTF	heat transfer fluid
LHTES	latent heat thermal energy storage
PCM	phase change material
TES	thermal energy storage

the large-scale energy usage, the heating requirements of the power cycle in the CSP need to be high to achieve high efficiencies. Moreover, in order to increase the storage capacity for large-scale electricity generation, high melting temperature (above 700 °C) PCMs are being considered for latent heat storage.

In the present study, magnesium chloride ($MgCl_2$) whose melting point is 714 °C [4] was chosen as the PCM for the TES system. Because of the low thermal conductivity of magnesium chloride, aligned ligament graphite foam was introduced to enhance the overall thermal conductivity of the graphite foam–PCM combination. The open porosity of the graphite foam is around 90%, i.e. 90% of volume is occupied by the PCM in the graphite foam–PCM combination. This study concentrated on analyzing the heat transfer performance and the exergy efficiency of the graphite foam–PCM LHTES system. The thermal performance of the storage system was analyzed under various situations through 3-D COMSOL heat transfer simulations.

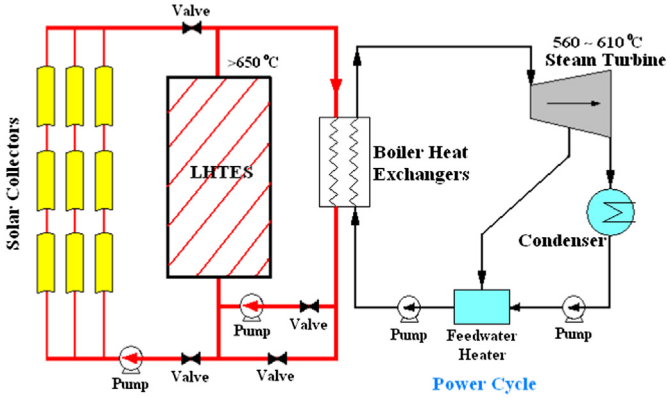

Fig. 1. Schematic of the energy flow in CSP with TES system.

Heat transfer studies are often intended to increase detailed understanding of the heat transfer performance in TES systems in order to help their design and optimization. Currently, there are many investigations into phase change phenomena in this area [5–10]. Nithyanandam and Pitchumani studied the heat transfer performances in a single PCM tube considering the effects of heat pipes and metal foam in the PCM [5]. Yang and Garimella have investigated the melting of a PCM in metal foams including buoyancy-driven convection in the liquid phase PCM in a square enclosure [6]. Lamberg et al. have studied the melting and freezing processes in a PCM both numerically and experimentally [7]. They considered the effects of fins in the PCM storage. For numerical simulations, they introduced two methods, an enthalpy method and an effective heat capacity method, and compared the results of both methods [7]. Li et al. studied melting/solidification problems for phase change using the front-tracking algorithm [8,9]. Voller et al. investigated convection/diffusion phase change problems with the enthalpy method [10]. Nevertheless, most of the investigators focused on a single PCM tube [5] or single PCM domain [6–10]. Few studies are for the storage system. Therefore, the present simulations concentrate on 3-D heat transfer in full scale LHTES tank systems (multiple-pipe systems).

Exergy is used to determine the reversible energy obtainable in thermal systems based on the second law of thermodynamics analysis. Exergy analysis can help the performance assessment and optimization of the TES system [11] and is receiving more and more attention recently. Some investigators have focused on the exergy analysis of overall solar power systems [12–14]. They have studied the exergy efficiencies of various parts in solar power plants, including the solar collector cycle and the power cycle. Some studies concentrated on the exergy efficiency of the solar collector cycle [15]. Other investigators calculated the exergy efficiency of cascading latent heat storage systems [15–17]. However, most of these studies have been applied to the exergy efficiency for low or medium operation temperature solar power systems [12–14,16,17]. Few investigators considered the exergy analysis for high-temperature latent heat storage systems. Moreover, the exergy effects of thermal conductivity enhancement with additives for PCMs have rarely been studied [11], and only a few investigators have analyzed the exergy for cascading PCMs [15–17]. Therefore, this study focused on the exergy efficiency of a high-temperature LHTES system. It included the exergy efficiencies for graphite foam–PCM combination storage systems as well as cascading latent heat storage systems.

2. Mathematical modeling

The LHTES system considered included a tank filled with graphite foam–PCM with the HTF flowing vertically upwards through pipes in the tank. A sketch of the latent heat storage system is displayed in Fig. 2. In order to analyze the heat transfer performance in the storage tank with the anisotropic thermal conductivity, 3-D numerical simulations were conducted using commercial software COMSOL. A similarity section, in terms of the hexagon storage volume shown in Fig. 2(b), was used for the simulations. The outer and inner diameters of the HTF pipes are 60.32 mm and 54.79 mm, respectively. The size of the HTF pipe was chosen based on the capital cost (in terms of the number and size of the pipes) and the operating cost (in terms of the pumping power requirements) [18]. Larger pipe sizes result in higher HTF flow rates with higher pumping power requirements and increase the operating costs for the storage system. Smaller pipe sizes significantly increase the total number of HTF pipes in the storage tank and thus increase the capital cost of the system. Therefore, the 60.32-mm outer diameter with 54.79-mm inner diameter pipe was selected as the near optimum HTF pipe size in the current LHTES system considering both capital cost and operating cost [18].

The plant electricity generation capacity was set at 100 MW with 12-h storage capacity. Supercritical steam was adopted for the power cycle for the high-temperature heating requirements of the power block for large-scale electricity generation. The efficiency of the power cycle using supercritical steam is as high as 45% [19]. Therefore, the storage capacity of the LHTES system is about 220 MW. The height of the latent heat storage tank was set at 10 m based on the height of the storage tank of Gemasolar in Spain [2]. The total mass of graphite foam–PCM combination is approximately 16,000 metric tons in order to achieve the storage capacity based on a graphite foam–$MgCl_2$ LHTES system (including both latent heat and sensible heat storage in the system). In order to have most of the PCM undergo phase change, the distance between HTF pipes was found to be about 0.54 m [18], which leads to approximately 4290 HTF pipes needed in the graphite foam–$MgCl_2$ storage tank system [18]. Under these conditions, the diameter of the storage tank would be 34.6 m to hold the total amount of graphite foam–PCM as well as the HTF pipes in the system.

The present study is intended to add to the understanding of the processes analyzed [18] by including the 3-D effects of the

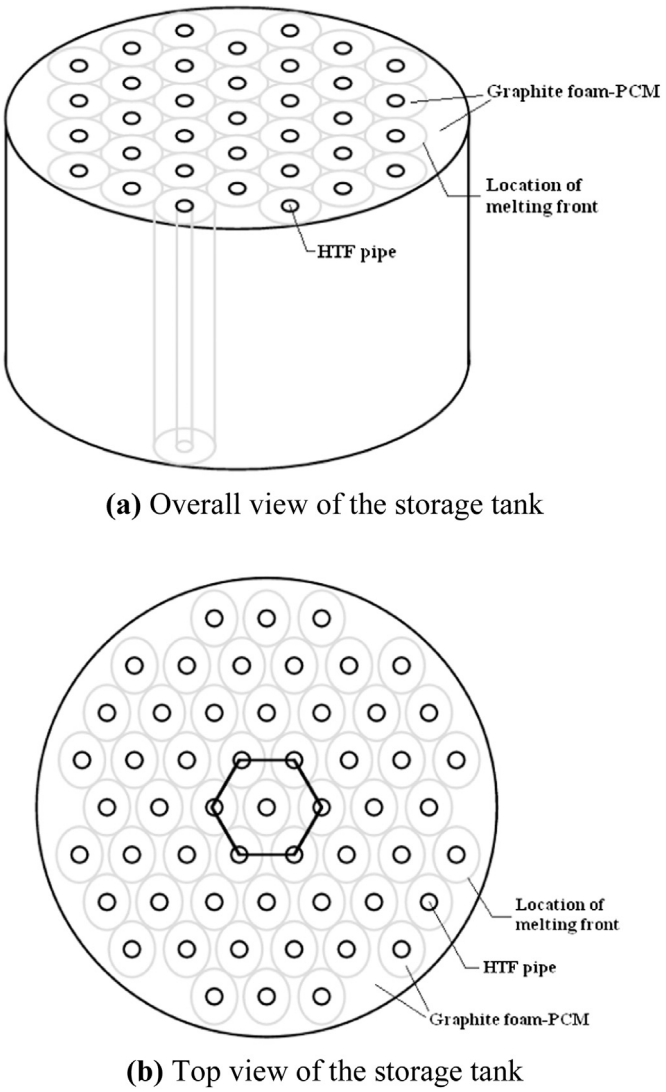

Fig. 2. Schematic of the latent heat storage system.

Table 1
Properties of graphite foam–$MgCl_2$, HTF, and fluid pipe [4,21–25].

	Density (kg/m^3)	Thermal conductivity (W/m K)	Heat capacity (kJ/kg K)	Latent heat of fusion (kJ/kg)	Dynamic viscosity (N s/m^2)
Graphite foam–$MgCl_2$ combination	1722 [4,22]	25 [4,22]	0.967 [21]	407.6 [4]	–
Liquid FLiNaK [23,24]	2018.9	0.921	1.89	–	0.0029
Inconel alloy 617 [25]	8360	24.2	0.586	–	–

graphite foam–$MgCl_2$ used for latent heat storage with a melting point of 714 °C. Exergy analysis is also introduced. The melting temperature range is around 30 K according to the differential scanning calorimetry (DSC) measurement for $MgCl_2$ [20]. In this study, liquid-state LiF–NaF–KF (46.5–11.5–42 mol%) (FLiNaK) was used as the HTF. Inconel alloy 617 was used as the heat transfer fluid pipe. The properties of the graphite foam–$MgCl_2$, the HTF, and the HTF pipe were found from Refs. [4,21–25], as given in Table 1. Temperature and direction dependencies were considered in the 3-D calculations and are described subsequently.

2.1. Heat transfer simulations

There were several assumptions adopted in the simulations described as follows:

- The LHTES system was well insulated.
- The HTF inlet temperature maintained at a constant value.
- The flow velocity maintained constant in the HTF pipes during charging or discharging processes.
- The buoyancy-driven convection in the liquid-phase PCM was neglected because it was not significant in the porous media.
- The volume change of the PCM due to the thermal expansion of materials during phase change was not considered.
- The thermal resistance of the gap between the HTF pipe and the graphite foam–PCM combination was neglected because it would be filled with brazing materials or the PCM.

The equivalent heat capacity method [26] was adopted for the phase change simulations in COMSOL. Thus, the energy equation for the phase change process is expressed as equation (1).

$$\rho c_p \frac{\partial T}{\partial t} = \nabla\cdot(k\nabla T) \tag{1}$$

where ρ is the density of graphite foam–PCM combination, c_p is the heat capacity of the combination, k is the thermal conductivity of the combination, T is the temperature, and t is the time.

The thermophysical properties of the graphite foam–PCM combination in equation (1) were determined as follows in the programming during the phase change process [27]:

$$k = k_s + (k_l - k_s)B(T) \tag{2}$$

$$\rho = \frac{\rho_l c_{p,l} B(T) + (1 - B(T))\rho_s c_{p,s}}{c_{p,l} B(T) + (1 - B(T))c_{p,s}} \tag{3}$$

$$c_p = c_{p,s} + \left(c_{p,l} - c_{p,s}\right)B(T) + L\frac{d\alpha}{dT} \tag{4}$$

where k_s and k_l are the thermal conductivities of solid and liquid state foam–PCM combinations, respectively, ρ_s and ρ_l are the densities of solid and liquid state foam–PCM combinations, respectively, $c_{p,s}$ and $c_{p,l}$ are the heat capacities of solid and liquid state foam–PCM combinations, respectively, and L is the latent heat of fusion of the graphite foam–PCM combination. In equation (4), $(d\alpha/dT)$ is the Gaussian function used to account for the latent heat of fusion [27]. It is equal to zero when the temperature of the graphite foam–PCM combination is above or below the melting temperature range of the PCM but nonzero when the temperature of the graphite foam–PCM combination is in the melting temperature range of the PCM (with its integral over the melting temperature range being equal to 1) [27]. The function $B(T)$ is the liquid fraction used to determine the change in k, ρ, and c_p between solid and liquid phases of the graphite foam–PCM combination and is defined by the following equation [27]:

$$B(T) = \begin{cases} 0 & T < (T_m - \Delta T) \\ \dfrac{T - T_m + \Delta T}{2\Delta T} & (T_m - \Delta T) \le T \le (T_m + \Delta T) \\ 1 & T > (T_m + \Delta T) \end{cases} \tag{5}$$

Here T_m is the melting point of graphite foam–$MgCl_2$ (714 °C) and $2 \times \Delta T$ is the melting temperature range of $MgCl_2$. According to the DSC measurement of the heat capacity and latent heat of $MgCl_2$, there is a 30-K melting range for phase change of $MgCl_2$ [20]. $B(T)$ is zero when the graphite foam–PCM temperature is lower than the melting temperature range indicating the PCM is in the completely solid state. $B(T)$ is unity when the graphite foam–PCM temperature is above the melting temperature range indicating the PCM is in the liquid state. $B(T)$ changes between zero and unity within the melting temperature range.

The internal flow convection inside HTF pipes was simulated by COMSOL based on the Sieder–Tate correlation [28]:

$$h = \begin{cases} \dfrac{k}{D}3.66 & Re_D \le 2500 \\ \dfrac{k}{D}0.027 Re_D^{4/5} Pr^n \left(\dfrac{\mu}{\mu_s}\right)^{0.14} & Re_D > 2500 \end{cases} \tag{6}$$

where h is the heat transfer coefficient, D is the inner diameter of the HTF pipe, Re_D is the Reynolds number, Pr is the Prandtl number, μ is the HTF dynamic viscosity, μ_s is the HTF viscosity at the wall temperature, and the exponent n is equal to 0.3 or 0.4 when the wall temperature is lower or higher than the fluid temperature, respectively.

2.2. Exergy analysis

There are two main methods to determine the exergy efficiency of the LHTES system. Equations to calculate the exergy efficiency are given as follows [11,15–17].

2.2.1. Overall exergy efficiency, $\psi_{overall}$ [11,15–17]

The first method to determine the exergy efficiency of the LHTES system is the overall exergy efficiency method, which is defined by equation (7). The overall exergy efficiency of the storage system includes the efficiencies of both the charging process (ψ_{char}) and the discharging process (ψ_{dis}) as expressed by equations (8) and (9).

$$\psi_{overall} = \psi_{char}\psi_{dis} \tag{7}$$

$$\psi_{char} = \frac{Ex_{PCM\_stored}}{Ex_{HTF\_char}} \tag{8}$$

$$\psi_{dis} = \frac{Ex_{HTF\_dis}}{Ex_{PCM\_supplied}} \tag{9}$$

Here the efficiency of the charging process (ψ_{char}) is determined by the total exergy stored in the graphite foam–PCM (Ex_{PCM_stored}) as a fraction of the total exergy supplied by the HTF (Ex_{HTF_char}) during the charging process. The exergy stored in the graphite foam–PCM (Ex_{PCM_stored}) is defined by equation (10). It includes the exergy stored during the melting as well as the

exergy stored during the sensible heating before and after the melting [11].

$$\mathrm{Ex}_{\mathrm{PCM\_stored}} = ML\left(1-\frac{T_a}{T_m}\right)+Mc_{p,s}\left[(T_m-T_{\mathrm{PCM,init}})-T_a\ln\left(\frac{T_m}{T_{\mathrm{PCM,init}}}\right)\right]+Mc_{p,l}\left[(T_{\mathrm{PCM,char}}-T_m)-T_a\ln\left(\frac{T_{\mathrm{PCM,char}}}{T_m}\right)\right] \tag{10}$$

where M is the total mass of the graphite foam–PCM combination in the storage system. T_a is the environmental temperature, which was taken as 20 °C, and T_m is the melting point of the PCM. Furthermore, $T_{\mathrm{PCM,init}}$ is the initial temperature of the graphite foam–PCM before the charging process. $T_{\mathrm{PCM,char}}$ is the final temperature of the graphite foam–PCM after the charging process.

The total exergy supplied by the HTF during the charging process ($\mathrm{Ex}_{\mathrm{HTF\_char}}$) in equation (8) is expressed as equation (11). The HTF inlet temperature ($T_{\mathrm{HTF\_char\_inlet}}$) was maintained at a constant value during the charging process while the HTF outlet temperature ($T_{\mathrm{HTF\_char\_outlet}}$) varied with time. Thus, the average HTF outlet temperature was used in the exergy efficiency calculations.

$$\mathrm{Ex}_{\mathrm{HTF\_char}} = \rho_{\mathrm{HTF}}AV_{\mathrm{HTF\_char}}c_{\mathrm{HTF}}\left[(T_{\mathrm{HTF\_char\_inlet}}-T_{\mathrm{HTF\_char\_outlet}})-T_a\ln\left(\frac{T_{\mathrm{HTF\_char\_inlet}}}{T_{\mathrm{HTF\_char\_outlet}}}\right)\right]t \tag{11}$$

Here ρ_{HTF} is the density of the HTF, c_{HTF} is the heat capacity of the HTF, A is the inner cross section area of the HTF pipe, $V_{\mathrm{HTF\_char}}$ is the charging HTF velocity, and t is the time.

The exergy efficiency of the discharging process (ψ_{dis}) is determined as the ratio of exergy recovered by the HTF ($\mathrm{Ex}_{\mathrm{HTF\_dis}}$) to the total exergy supplied by the graphite foam–PCM ($\mathrm{Ex}_{\mathrm{PCM\_supplied}}$) as expressed in equation (9). The exergy supplied by the graphite foam–PCM is illustrated in equation (12). $T_{\mathrm{PCM,dis}}$ is the final temperature of graphite foam–PCM after the discharging process. Because $T_{\mathrm{PCM,char}}$ and $T_{\mathrm{PCM,dis}}$ varied in the radial direction as well as in the axial direction (along the HTF pipe) in the graphite foam–PCM, the average $T_{\mathrm{PCM,char}}$ and $T_{\mathrm{PCM,dis}}$ in the storage system were used in the exergy simulations.

$$\mathrm{Ex}_{\mathrm{PCM\_supplied}} = ML\left(1-\frac{T_a}{T_m}\right)+Mc_{p,s}\left[(T_m-T_{\mathrm{PCM,dis}})-T_a\ln\left(\frac{T_m}{T_{\mathrm{PCM,dis}}}\right)\right]+Mc_{p,l}\left[(T_{\mathrm{PCM,char}}-T_m)-T_a\ln\left(\frac{T_{\mathrm{PCM,char}}}{T_m}\right)\right] \tag{12}$$

The exergy retrieved to the HTF during discharging process ($\mathrm{Ex}_{\mathrm{HTF\_dis}}$) is illustrated in equation (13). The HTF inlet temperature during the discharging process ($T_{\mathrm{HTF\_dis\_inlet}}$) was also maintained at a constant value while the HTF outlet temperature during the discharging processes ($T_{\mathrm{HTF\_dis\_outlet}}$) varied with time. The average HTF outlet temperature during the discharging process was used as well.

$$\mathrm{Ex}_{\mathrm{HTF\_dis}} = \rho_{\mathrm{HTF}}AV_{\mathrm{HTF\_dis}}c_{\mathrm{HTF}}\left[(T_{\mathrm{HTF\_dis\_outlet}}-T_{\mathrm{HTF\_dis\_inlet}})-T_a\ln\left(\frac{T_{\mathrm{HTF\_dis\_outlet}}}{T_{\mathrm{HTF\_dis\_inlet}}}\right)\right]t \tag{13}$$

The overall exergy efficiency (ψ_{overall}) involves the exergy input and output of both the HTF and the graphite foam–PCM in the storage system.

2.2.2. Round trip efficiency, ψ_{round} [11,17]

The second method to determine the exergy efficiency in the storage system is the round trip efficiency method. The round trip exergy efficiency of the storage system is defined as the exergy recovered from the HTF during the discharging process as a fraction of the total exergy supplied to the HTF during the charging process which is expressed in equation (14) [11].

$$\psi_{\mathrm{round}} = \frac{\mathrm{Ex}_{\mathrm{HTF\_dis}}}{\mathrm{Ex}_{\mathrm{HTF\_char}}} \tag{14}$$

The storage system was assumed to be well insulated. Therefore, the heat loss from the LHTES system is negligible in the current exergy analysis. Thus, the two exergy efficiency analysis methods are the same because there is no heat loss from the graphite foam–PCM between the charging process and the discharging process. Therefore, the round trip exergy efficiency method was adopted to analyze the exergy efficiency in the current LHTES system.

For the charging process, the HTF velocity was set at 0.15 m/s to maintain a low Reynolds number (~5700) turbulent flow in the pipes based on the heat transfer performance in the graphite foam–PCM and the pumping power requirement of the system [18]. The inlet HTF temperature during the charging process was fixed at 820 °C, and the initial graphite foam–PCM temperature was 620 °C before the charging process. The operation time for the energy storage process is 8 h. For the discharging process, the discharging HTF inlet temperatures were adjusted to retrieve the total energy stored in the graphite foam–PCM during the previous charging process. The flow velocity was 0.1 m/s for the discharging process with Re_D around 3800, and the operation time was 12 h.

3. Model verification

Before running the 3-D simulations, the 3-D COMSOL numerical simulation for the energy storage process using the equivalent heat capacity method was compared to a one-dimensional (1-D) heat transfer simulation using the front-tracking method [8,9,29,30] (governing equations combined with boundary conditions were solved by the finite difference method) to provide a measure of verification of the COMSOL simulations. The front-tracking method [29,30] is for a sharp phase transition, and as part of this study, a numerical simulation was written specifically for this problem. Therefore, the melting temperature range was set to be very small in the COMSOL simulations (2 K) to create a sharp phase transition of the graphite foam–$MgCl_2$ combination.

For the 3-D COMSOL comparison simulation, the single HTF pipe model was applied to compare with the 1-D heat transfer simulation results. The temperature variations in the axial direction (along the HTF pipe) were considered as well as the heat conduction in the radial direction and angular direction in the 3-D model. The HTF inlet temperature was maintained at 820 °C during the charging process. The initial graphite foam–$MgCl_2$ combination temperature was at 620 °C. The 3-D single pipe model consists of 518,571

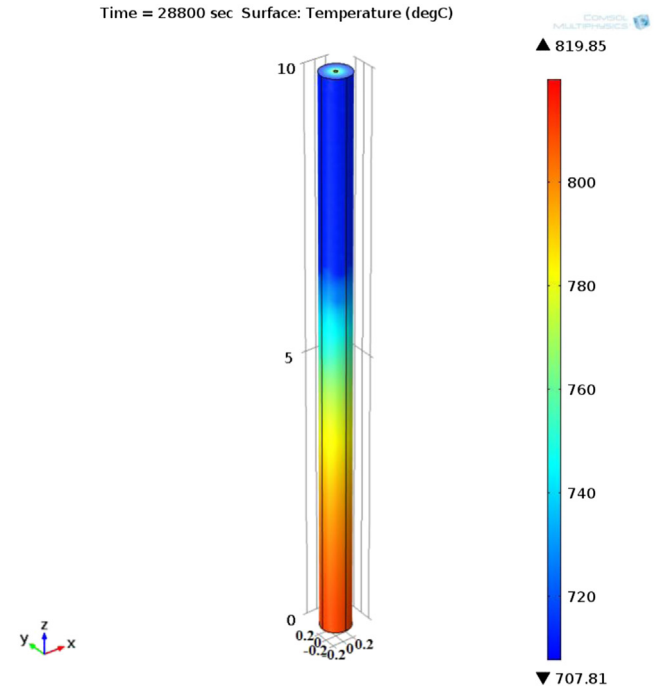

(a) Overall view of the 3-D model

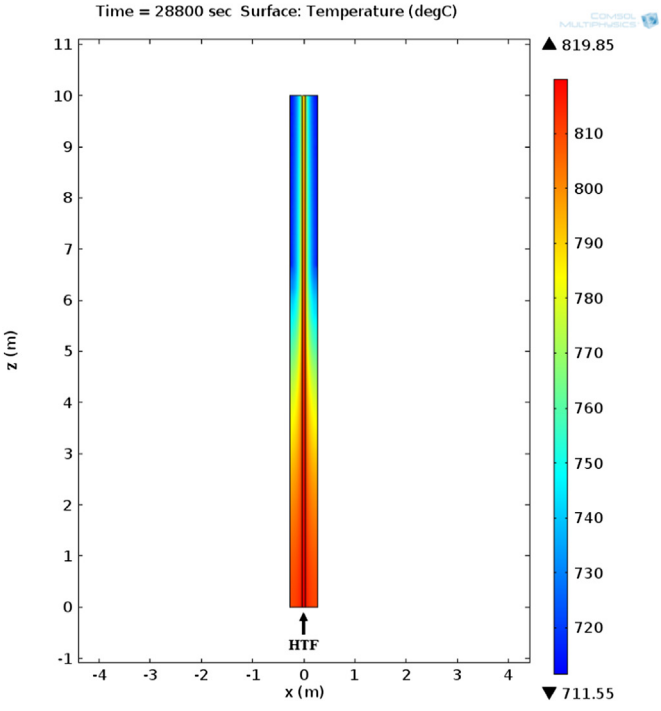

(b) Longitudinal section view of the 3-D model

Fig. 3. Temperature profiles in the graphite foam–$MgCl_2$ (single pipe system).

domain elements, 49,416 boundary elements, and 5928 edge elements, which are sufficient for the current heat transfer simulations. Fig. 3 shows the temperature profiles in the graphite foam–PCM as well as in the HTF after the 8-h charging process for the 3-D COMSOL simulation. The HTF temperature would decrease along the HTF pipe, as shown in Fig. 3(b) the longitudinal section view. Therefore, the temperatures are higher at the bottom area and relatively lower at the top area in the graphite foam–$MgCl_2$.

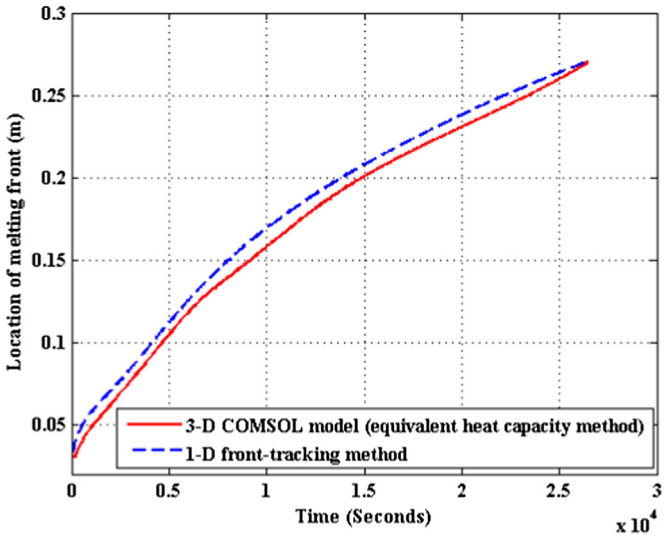

(a) Location of the melting front

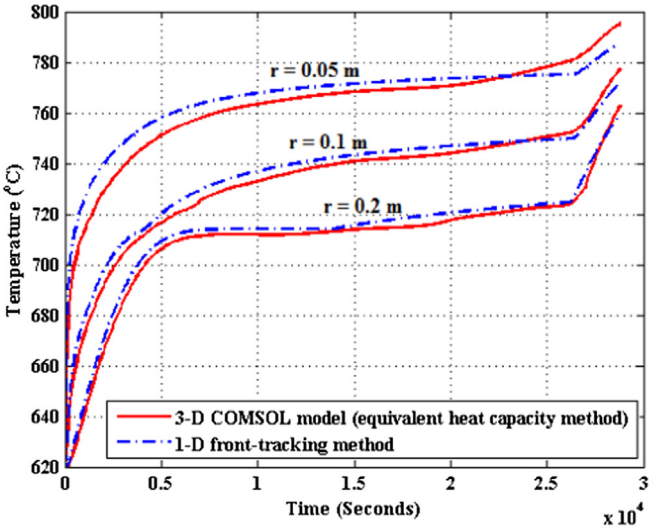

(b) Temperature profiles at various locations

Fig. 4. Comparison results between the 3-D COMSOL model using the equivalent heat capacity method and the 1-D front-tracking method.

For the 1-D simulation, it was assumed that the temperatures in the HTF and graphite foam–PCM were uniform in both the angular direction and the axial direction. Thermal gradients were only considered in the radial direction. Because the HTF temperature decreases along the HTF pipe during the charging process as displayed in Fig. 3(b), the average HTF temperature in the HTF pipe was exported from the 3-D model and used for the 1-D simulation. The initial graphite foam–$MgCl_2$ temperature was still 620 °C. The radius of the graphite foam–PCM combination was 0.27 m (half of the distance between two HTF pipes). In determining the heat flux at the boundary inside the HTF pipe, the average heat transfer coefficient along the HTF pipe in the 3-D model was calculated and applied to the 1-D simulation model. The boundary at a radius of 0.27 m was assumed to be insulated. There was no heat flux through this boundary because of the symmetric geometry between two HTF pipes. The total charging process time was 8 h.

The locations of the melting front and the temperature profiles in the graphite foam–$MgCl_2$, calculated by the 3-D model at the axial midpoint of the storage tank were used to compare with the

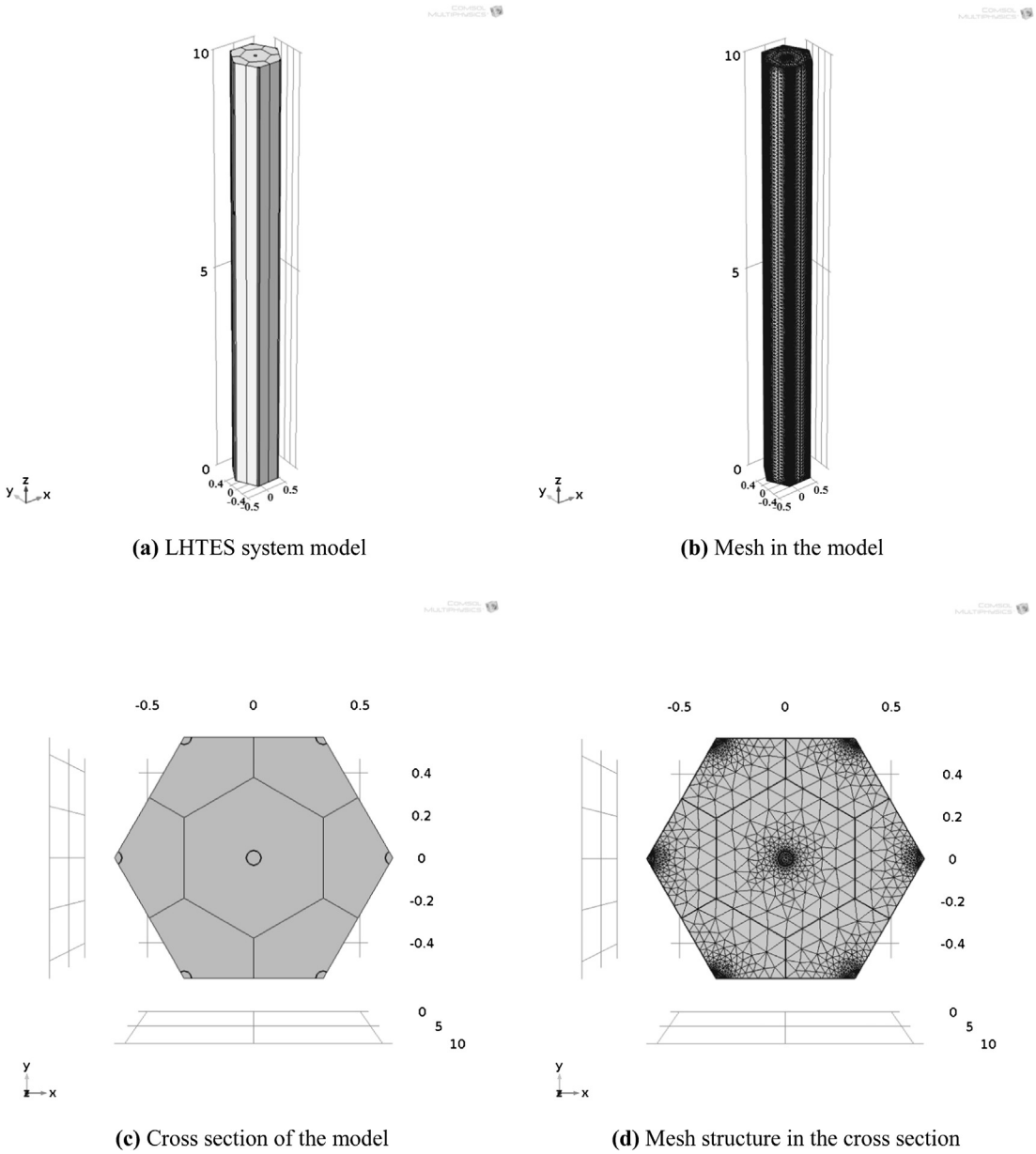

(a) LHTES system model

(b) Mesh in the model

(c) Cross section of the model

(d) Mesh structure in the cross section

Fig. 5. Simulation model of the LHTES system.

1-D simulation results, as displayed in Fig. 4. The temperature profiles from the 3-D model are very close (within 5%) to the temperature profiles from the 1-D simulation model according to Fig. 4(b). A smaller radius indicates a position closer to the HTF pipe while a larger radius indicates farther from the HTF pipe. The temperature is higher at the location closer to the pipe during the charging process. Furthermore, the locations of the melting fronts obtained from both methods are compared in Fig. 4(a). The melting fronts from both methods agree quite well with each other (within 5%). The melting front calculated from the 3-D model reaches the outer boundary ($r = 0.27$ m) at 7.35 h during the charging process while it takes about 7.3 h for the melting front to reach the outer boundary according to the 1-D simulation.

The melting fronts as well as the temperature profiles from the 3-D COMSOL model (the average results from the 3-D model) are quite close to the results from the 1-D simulation using the front-tracking method (within 5%). These results serve to verify the 3-D model, with its nodal mesh and time steps, for use in the analysis of phase change simulations to predict the heat transfer performance in the graphite foam–PCM LHTES system during the energy storage/retrieval process.

4. Results and discussions

The inlet temperature of the supercritical steam turbine is expected to be in the range of 560–610 °C [19]. Then the temperature difference between the HTF outlet and the steam turbine inlet is typically in the range of 15–45 °C [12–14,31,32]. Therefore, the HTF outlet temperature during the discharging process should be above 650 °C to achieve the maximum steam turbine inlet temperature (610 °C). The HTF velocity was selected based on the low Reynolds number turbulent flow in the HTF pipes of an outer diameter 60.32 mm and an inner diameter 54.97 mm. The flow velocity was 0.15 m/s during the charging process with 8-h energy storage time

and an HTF inlet temperature of 820 °C. The initial graphite foam–PCM temperature was 620 °C. For the discharging process, the flow velocity was 0.1 m/s with 12-h energy retrieval time. In these 3-D simulations, the anisotropic graphite thermal conductivities were included as well as the axial thermal gradient in the HTF and the melting temperature range of the graphite foam–PCM.

Fig. 5 shows the simulation model of the graphite foam–$MgCl_2$ LHTES system. The similarity section includes a full center HTF pipe and six partial pipes in a hexagonal arrangement. The rest of the volume is graphite foam–PCM combination. The model consists of 3,633,831 domain elements, 466,986 boundary elements, and 49,622 edge elements. Based on a mesh independence study, these mesh elements are sufficient in the 3-D numerical simulations for the storage system.

4.1. Heat transfer analysis

3-D simulations were performed in three groups for the LHTES system. First the system was analyzed for the PCM without graphite foam. Then the graphite foam–PCM system was considered using average material properties from Table 1, and finally both temperature dependence and anisotropic behavior of the material properties were added.

4.1.1. $MgCl_2$ without graphite foam

To quantify the effectiveness of the graphite foam in the LHTES system, the system was analyzed without the graphite foam to form a basis for comparison. Quantitative results are shown in Fig. 6 for the location of the melting front in pure $MgCl_2$ after the 8-h energy storage process. The thermal conductivity of $MgCl_2$ is very low. Consequently, the heat transfer performance in $MgCl_2$ is very poor as displayed in Fig. 6. The dark red (in the web version) region indicates the liquid-state PCM while the dark blue (in the web version) region represents the solid-state PCM. It is seen that only a small amount of the PCM melted after the 8-h energy storage process. In terms of required HTF pipes for the thermal capacity of the LHTES system, 40,089 heat transfer fluid pipes are required when the graphite foam is not applied in the system. It should be noted that neglecting natural convection in the PCM without foam reduces the accuracy of the calculations somewhat. However, it does not change the conclusion that the number of pipes increases by an order of magnitude without foam.

4.1.2. Graphite foam–$MgCl_2$ combination

After an 8-h energy storage process using average material properties, the location of the melting front and the temperature profiles in the graphite foam–$MgCl_2$ combination are displayed in Fig. 7. Fig. 7(a), (c) and (e) shows the melting front between the solid-state and liquid-state PCMs in the overall view, cross section view, and longitudinal section view, respectively. In the melting-front figures, a value of one indicates completely liquid-state PCM (dark red, in the web version) while zero represents completely solid-state PCM (dark blue, in the web version). Based on the COMSOL simulations, most of the $MgCl_2$ was melted after the 8-h charging process with the exception of a small part of the $MgCl_2$ at the top half of the storage system as shown in the longitudinal section view of Fig. 7(e). The very top of the LHTES system has the most unmelted PCM after the energy storage process, as displayed in Fig. 7(c) (blue regions, in the web version), which are furthest from the HTF pipes and in the region of the coldest HTF. A higher HTF temperature or a closer HTF pipe distance can be introduced to reduce this condition at an additional expense. Fig. 7(b), (d) and (f) displays the isothermal temperature contours in the storage system. Because the HTF flows from the bottom to the top of the storage system, the highest temperature of the PCM occurs at the bottom area and decreases axially along the pipes as well as radially. The results of Fig. 7 show symmetry among the HTF pipes due to the average property values used from Table 1. Because the thermal conductivity of graphite foam–$MgCl_2$ combination is very high as illustrated in Table 1, the heat transfer performance in the combination is quite good compared to the pure $MgCl_2$ storage system without the graphite foam of Fig. 6.

4.1.3. Anisotropic aligned ligament graphite foam

The actual thermal conductivity of the infiltrated foam (the graphite foam–$MgCl_2$ combination) is different in the x, y, and z directions [20]. It is higher in one direction, and half of that value in the other two directions. In the following simulations, this anisotropic behavior was included, and both the thermal conductivity (W/m K) and the heat capacity (J/kg K) of the graphite foam–$MgCl_2$

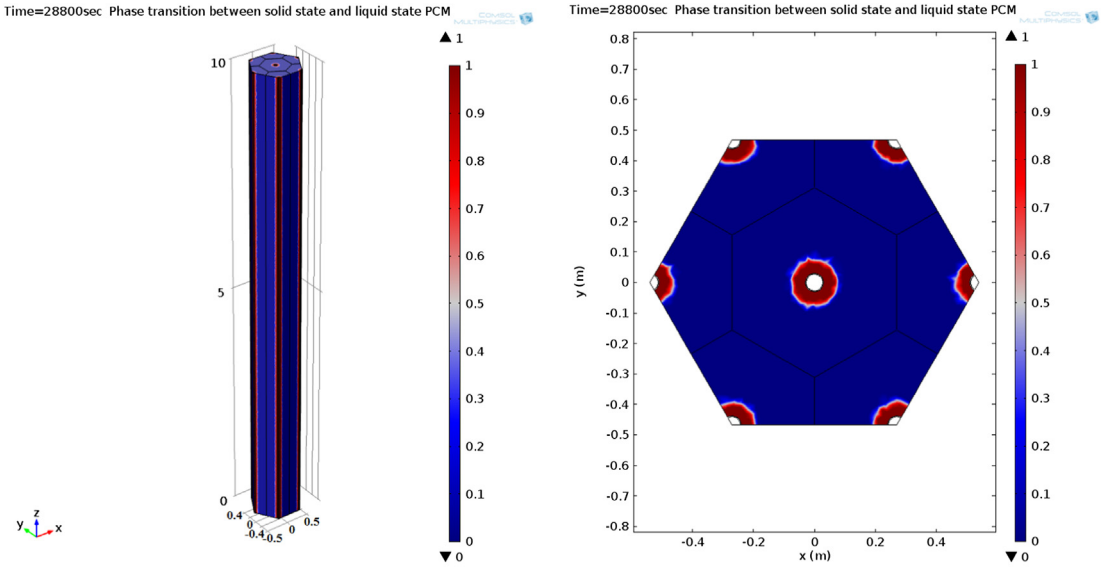

(a) Overall view **(b)** Cross section view

Fig. 6. Locations of the melting front in $MgCl_2$ without graphite foam after the 8-h charging process.

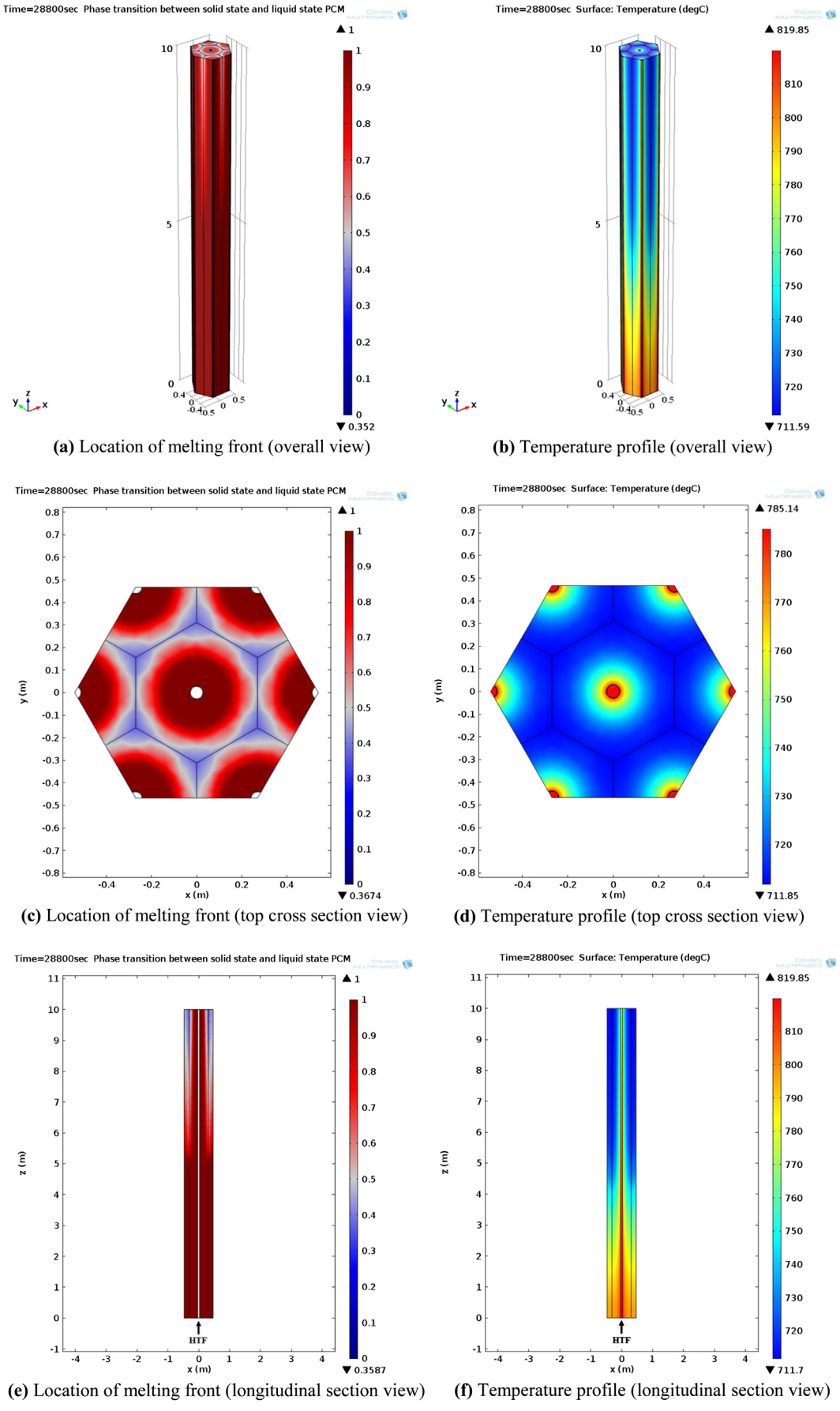

(a) Location of melting front (overall view)

(b) Temperature profile (overall view)

(c) Location of melting front (top cross section view)

(d) Temperature profile (top cross section view)

(e) Location of melting front (longitudinal section view)

(f) Temperature profile (longitudinal section view)

Fig. 7. Locations of the melting front and temperature profiles in the graphite foam–$MgCl_2$ LHTES system after the 8-h charging process.

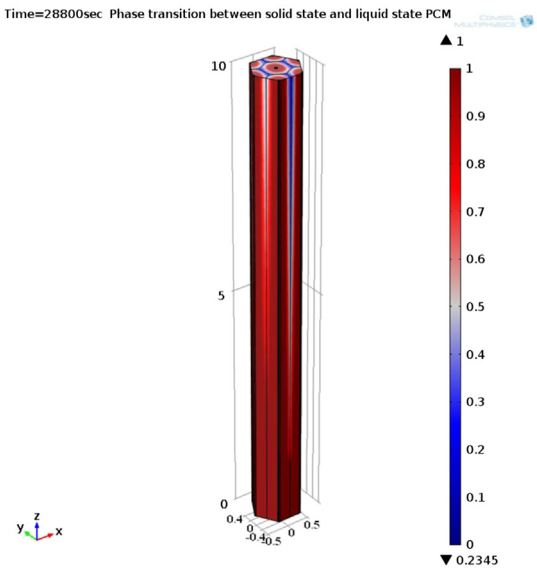

(a) Location of melting front (overall view)

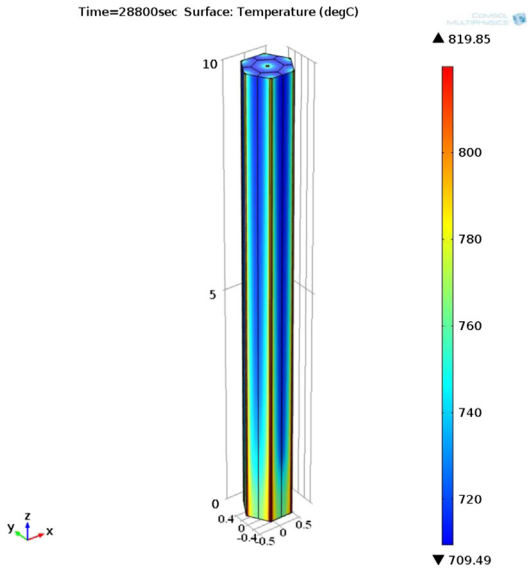

(b) Temperature profile (overall view)

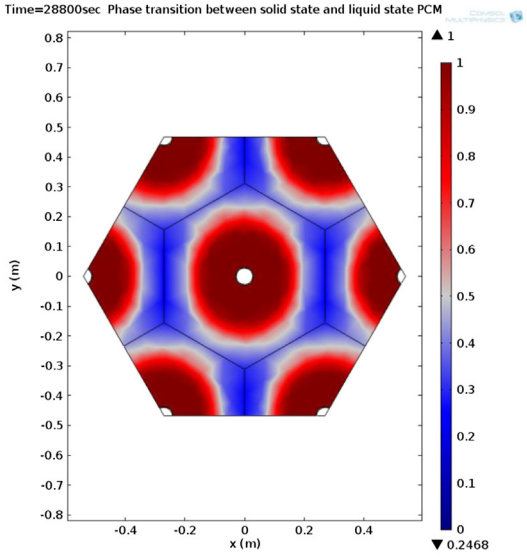

(c) Location of melting front (top cross section view)

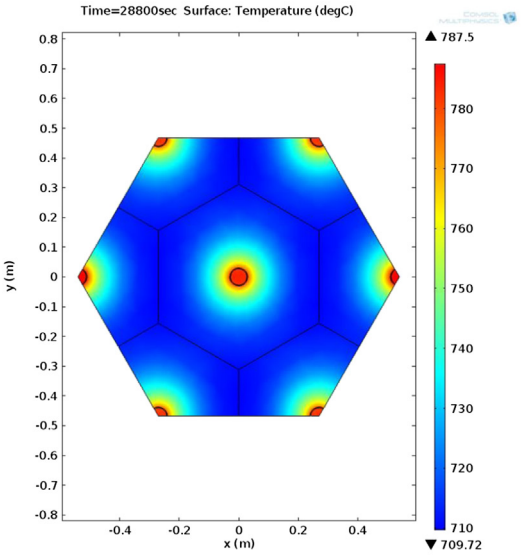

(d) Temperature profile (top cross section view)

Fig. 8. Melting fronts and temperature contours in the graphite foam–$MgCl_2$ combination after the 8-h charging process (with different thermal conductivities in different directions).

were treated as a function of the temperature (K) through equations (15)–(18) [20].

$$k_{\text{combination\_}y} = 58.5 - 0.0313 \times T \tag{15}$$

$$k_{\text{combination\_}x} = k_{\text{combination\_}z} = \frac{k_{\text{combination\_}y}}{2} \tag{16}$$

$$c_{p,s} = 650.24 + 0.5317 \times T - 1.3444 \times 10^{-4} \times T^2 \tag{17}$$

$$c_{p,l} = 752.5 + 0.389 \times T - 1.3444 \times 10^{-4} \times T^2 \tag{18}$$

Equations (14) and (15) were used for the thermal conductivity of the graphite foam–$MgCl_2$ for both solid and liquid phases [20]. In order to take advantage of the higher thermal conductivity direction in the LHTES system, the higher value was fixed in the *y* direction perpendicular to the axis of the HTF pipes. The thermal conductivity in the *x* and *z* directions was set to half of the value in the *y* direction. These values were used to replace the constant thermal conductivity value of the graphite foam–$MgCl_2$ combination in Table 1, which is very close to the higher thermal conductivity of the infiltrated foam (*y* direction).

Results, from the numerical simulations using the anisotropic thermal conductivity and the temperature-dependent thermal conductivity and specific heat, are given in Fig. 8 where the melting front and the temperature profiles in the foam–PCM combination are shown. By comparing the results of Figs. 7 and 8, it is clear that the results are less symmetric in Fig. 8 due to the anisotropic thermal conductivity. In Fig. 8 it is seen that there is more solid PCM in the *x*-direction than in the *y*-direction, with its higher thermal conductivity, after the 8-h energy storage process. Although the thermal conductivity of the infiltrated foam (the graphite foam–$MgCl_2$ combination) is two times higher in the *y* direction than in

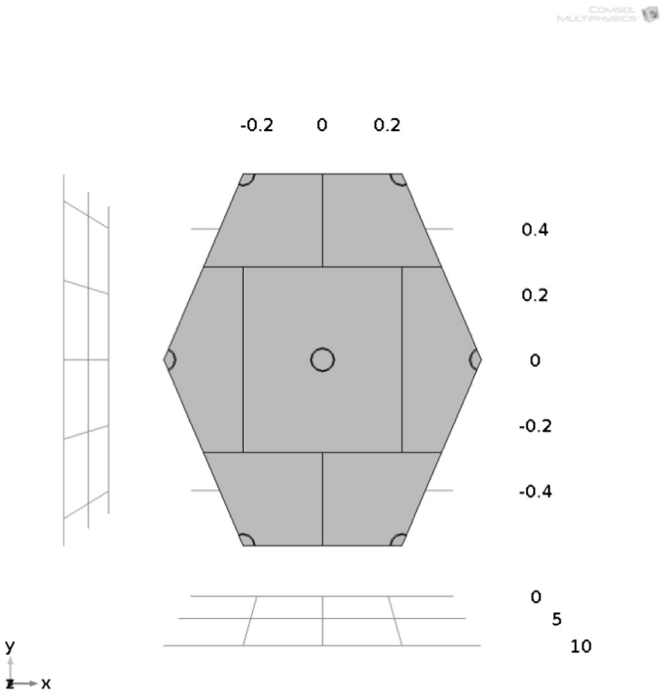

Fig. 9. Cross section of the modified model to make all the PCM in the storage system melt during the energy storage process.

the *x* direction, the ratio of the melting fronts between the two directions is not 2 to 1. For the top of the storage system, the melting front in the *y* direction reaches 0.234 m while the melting front in the *x* direction is 0.193 m, as displayed in Fig. 8(c). This result indicates that significant heat transfer occurred in the circumferential direction through the graphite ligaments producing a somewhat symmetrical result similar to Fig. 7. The temperature contour at the cross section in Fig. 8(d) illustrates that the temperature distribution is also relatively uniform in the anisotropic graphite foam–$MgCl_2$ combination.

Using average thermal property results from Fig. 7, approximately 4290 HTF pipes are needed in the storage tank to achieve the required storage capacity in the LHTES system. However, considering the actual temperature-dependent and anisotropic properties of the graphite foam–$MgCl_2$ combination results in changes shown in Fig. 8. Compared to Fig. 7(c), there is more PCM in the storage system wasted as shown in Fig. 8(c) because it does not experience phase change. In order for all of the PCM to melt during the energy storage process, more HTF pipes could be introduced in the thermal storage system, especially in the *x* direction. One option is keeping the pipe distance in the *y* direction the same while reducing the pipe distance in the *x* direction from 0.54 m to 0.4 m as illustrated in Fig. 9. To obtain the same storage capacity, approximately 5293 HTF pipes are needed in the storage system of Fig. 9 based on simulations, increasing around 1000 pipes in the storage tank, compared to approximately 40,000 HTF pipes in the pure $MgCl_2$ TES system without the graphite foam as described in Section 4.1.1. Thus, the use of the graphite foam with the PCM has the dramatic effect on reducing the number of required HTF pipes in the LHTES system by a factor of about 8 compared to using the PCM alone.

4.2. Exergy analysis

Constant thermophysical properties of the graphite foam–$MgCl_2$, as displayed in Table 1, were used for the exergy simulations. By using the results for Fig. 6, the distance between HTF pipes was 0.54 m in the storage tank system with a height of 10 m. The round trip exergy efficiencies under various situations were calculated by using equations (11), (13) and (14) to evaluate the thermal performance of the storage system. The results for three cases are given in Table 2. The round trip exergy efficiency includes the entropy generation in both charging and discharging processes. It was assumed that the LHTES system is well insulated. Therefore, the heat loss from the storage system is negligible in the current exergy analysis.

Case 1 is the graphite foam–$MgCl_2$ combination latent heat storage system analyzed previously for heat transfer. The round trip exergy efficiency of the graphite foam–$MgCl_2$ system is quite high at 96.8%. The average discharging HTF outlet temperature is above 660 °C. Thus, it can achieve the requirement of the supercritical steam turbine in the power cycle.

Case 2 is for a cascading latent heat storage system. KCl and $MgCl_2$ are used as the cascaded PCMs with different melting points. The melting point of KCl is 770 °C while the melting point of $MgCl_2$ is 714 °C [4]. The thermophysical properties of the graphite foam–KCl are given in Table 3. Half of the volume of the storage system is occupied by the graphite foam–KCl, and the other half of the volume by the graphite foam–$MgCl_2$ as shown in Fig. 10. Fig. 10 also shows the melting front in the cascading graphite foam–PCMs after the 8-h energy storage process. A cascading PCM system can improve the exergy efficiency of the latent heat storage system because it has more uniform temperature differences between the HTF and the melting points of the PCMs along the thermocline compared to a non-cascaded system [17]. The exergy efficiency calculated for the cascading PCMs in this case is very high at 97.8%, as seen in Table 2. As expected, the cascading system shows an improvement over the non-cascading system, but it is small. This result is due to the exergy efficiency of the non-cascading system being very high itself. Moreover, the cascading graphite foam–PCM system can also reach the desired outlet temperature to match the supercritical steam turbine temperature in the power cycle.

Table 2
Exergy efficiency in the latent heat storage system.

	Round trip exergy efficiency, ψ_{round}
Case 1	
Graphite foam–$MgCl_2$	96.8%
8-h charging, inlet temp. 820 °C	
Average outlet temp. 765.0 °C	
$V_{HTF\_char} = 0.15$ m/s	
12-h discharging, inlet temp. 607 °C	
Average outlet temp. 664.0 °C	
$V_{HTF\_dis} = 0.1$ m/s	
Case 2	
Cascading PCMs: KCl and $MgCl_2$ (with graphite foam)	97.8%
8-h charging, inlet temp. 820 °C	
Average outlet temp. 773.5 °C	
$V_{HTF\_char} = 0.15$ m/s	
12-h discharging, inlet temp. 616 °C	
Average outlet temp. 664.6 °C	
$V_{HTF\_dis} = 0.1$ m/s	
Case 3	
PCM: $MgCl_2$ (without graphite foam)	67.7%
8-h charging, inlet temp. 820 °C	
Average outlet temp. 811.9 °C	
$V_{HTF\_char} = 0.15$ m/s	
12-h discharging, inlet temp. 578 °C	
Average outlet temp. 584.1 °C	
$V_{HTF\_dis} = 0.1$ m/s	

Table 3
Thermophysical properties of graphite foam–KCl [4,22].

	Density (kg/m^3)	Thermal conductivity (W/m K)	Heat capacity (kJ/kg K)	Latent heat of fusion (kJ/kg)
Graphite foam–KCl combination	1578	25	0.988	320.7

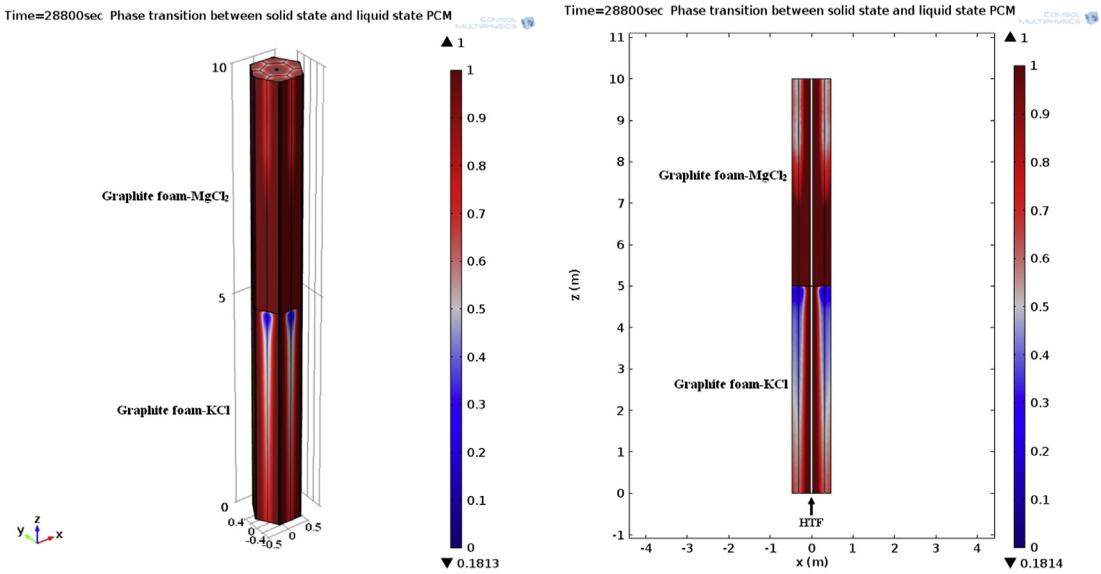

(a) Overall view **(b)** Longitudinal section view

Fig. 10. Locations of the melting front in the cascading LHTES system after the 8-h energy storage process.

Case 3 is for the $MgCl_2$ latent heat storage system without the graphite foam, the thermal conductivity enhancement additive. The round trip exergy efficiency is just 67.7% when there is no graphite foam in the PCM. Because the thermal conductivity of $MgCl_2$ is low, a lot of the PCM does not melt during the charging process. Therefore, the total latent heat energy stored in the system due to phase change is very small compared to the graphite foam–$MgCl_2$ system under the same conditions. Thus, the overall exergy efficiency decreases significantly in the $MgCl_2$ storage system (without graphite foam). Furthermore, the average discharging HTF outlet temperature is just 584.1 °C for the non-graphite foam system, which is less than the 650 °C needed to match the maximum power cycle requirement (the maximum steam turbine inlet temperature being 610 °C). Based on the exergy analysis, it is clear that the graphite foam enhanced the exergy efficiency of the latent heat storage system remarkably.

5. Conclusions

Graphite foam was analyzed as the thermal conductivity enhancement additive of an LHTES system for a CSP plant. The plant considered was capable of producing high-temperature steam up to 610 °C in a supercritical power cycle. It was found that the graphite foam considerably improved the thermal performance in the LHTES system. The results of 3-D heat transfer simulations using average material properties showed that the melting front in a graphite foam–$MgCl_2$ combination can move much further compared to that in the $MgCl_2$ without the graphite foam during an 8-h charging process.

The accuracy of the heat transfer analysis was improved by including the anisotropic properties of the aligned ligament graphite foam as well as temperature dependence of the material properties. Although the thermal conductivity differed by a factor of two in different directions in the graphite foam, it was found that the effect on the temperature and melting front asymmetries was much less. This result is a consequence of relatively high heat transfer rates along the graphite ligaments. It was shown that some further improvement in the LHTES system could be achieved by changing the arrangement of the HTF pipes in the tank to take advantage of the anisotropic thermal conductivity, but the improvement is not substantial. In this case, the number of HTF pipes was found to decrease by a factor of eight from 40,000 to 5000 pipes. This result corresponds to a significant cost reduction in the LHTES system for the plant.

Exergy analyses of the LHTES system were performed with and without the graphite foam. The graphite foam was shown to increase the round trip exergy efficiency from 68% to 97%. The effect of cascading the graphite foam–PCM combination in the LHTES system was also considered from an exergy standpoint. Although the cascading improved the exergy efficiency, the improvement was small because the non-cascaded system exergy efficiency was very high at 97%.

Acknowledgements

This work was sponsored by the Solar Energy Technologies Program (Sunshot Initiative) of the U.S. Department of Energy under contract number DE-AC02-06CH11357 at Argonne National Laboratory, managed by UChicago Argonne LLC. Authors are grateful for helpful insights from Joseph Stekli and Levi Irwin of DOE.

References

[1] Kuravi S, Trahan J, Goswami DY, Rahman MM, Stefanakos EK. Thermal energy storage technologies and systems for concentrating solar power plants. Prog Energy Combust Sci 2013;39:285–319.

[2] Burgaleta JI, Arias S, Ramirez D. Gemasolar, the first tower thermosolar commercial plant with molten salt storage. Torresol Energy, Spain.
[3] Medrano M, Gil A, Martorell I, Potau X, Cabeza LF. State of the art on high-temperature thermal energy storage for power generation. Part 2 – case studies. Renew Sustain Energy Rev 2010;14:56–72.
[4] Janz GJ, Allen CB, Bansal NP, Murphy RM, Tomkins RPT. Physical properties data compilations relevant to energy storage. II. Molten salts: data on single and multi-component salt systems. Washington, D.C.: U.S. Department of Commerce, National Bureau of Standards; 1979.
[5] Nithyanandam K, Pitchumani R. Design and analysis of metal foam enhanced latent thermal energy storage with embedded heat pipes for concentrating solar power plants. In: Proceedings of ASME 2013, 7th international conference on energy sustainability and 11th fuel cell science, engineering and technology conference, Minneapolis, MN, USA: July 14–19; 2013.
[6] Yang Z, Garimella SV. Melting of phase change materials with volume change in metal foams. J Heat Transfer 2010;132:062301-1–062301-11.
[7] Lamberg P, Lehtiniemi R, Henell AM. Numerical and experimental investigation of melting and freezing processes in phase change material storage. Int J Therm Sci 2004;43:277–87.
[8] Li CY, Garimella SV, Simpson JE. A fixed-grid front-tracking algorithm for solidification problems. Part I – method and validation. Numer Heat Transfer B 2003;43:117–41.
[9] Li CY, Garimella SV, Simpson JE. A fixed-grid front-tracking algorithm for solidification problems. Part II – directional solidification with melt convection. Numer Heat Transfer B 2003;43:143–66.
[10] Voller VR, Cross M, Markatos NC. An enthalpy method for convection/diffusion phase change. Int J Numer Methods Eng 1987;24:271–84.
[11] Jegadheeswaran S, Pohekar SD, Kousksou T. Exergy based performance evaluation of latent heat thermal storage system: a review. Renew Sustain Energy Rev 2010;14:2580–95.
[12] Singh N, Kaushik SC, Misra RD. Exergetic analysis of a solar thermal power system. Renew Energy 2000;19:135–43.
[13] You Y, Hu EJ. A medium-temperature solar thermal power system and its efficiency optimization. Appl Therm Eng 2002;22:357–64.
[14] Xu C, Wang Z, Li X, Sun F. Energy and exergy analysis of solar power tower plants. Appl Therm Eng 2011;31:3904–13.
[15] Li Y, He Y, Wang Z, Xu C, Wang W. Exergy analysis of two phase change materials storage system for solar thermal power with finite-time thermodynamics. Renew Energy 2012;39:447–54.
[16] Watanabe T, Kanzawa A. Second law optimization of a latent heat storage system with PCMs having different melting points. Heat Recov Syst CHP 1995;15(7):641–53.
[17] Shabgard H, Robak CW, Bergman TL, Faghri A. Heat transfer and exergy analysis of cascaded latent heat storage with gravity-assisted heat pipes for concentrating solar power applications. Sol Energy 2012;86:816–30.
[18] Kim T, France DM, Yu W, Zhao W, Singh D. Heat transfer analysis of a latent heat thermal energy storage system using graphite foam for concentrated solar power. Sol Energy 2014;103:438–47.
[19] Gary J. CSP & the SunShot initiative. In: DOE-CSP industry meeting. Solar energy technologies program. U.S. Department of Energy; 2011.
[20] Properties of graphite foam–$MgCl_2$ with temperature provided by Ohio Aerospace Institute
[21] Janz GJ. Molten salts handbook. New York: Academic Press; 1967.
[22] Poling BE, Thomson GH, Friend DG, Rowley RL, Wilding WV. Perry's chemical engineers' handbook. 8th ed. New York: McGraw-Hill; 2008.
[23] Forsberg CW, Peterson PF, Zhao H. High-temperature liquid-fluoride-salt closed-Brayton-cycle solar power towers. J Sol Energy Eng 2007;129:141–6.
[24] Sohal MS, Ebner MA, Sabharwall P, Sharpe P. Engineering database of liquid salt thermophysical and thermochemical properties. Idaho National Laboratory; 2010.
[25] Inconel alloy 617. Special Metals Corporation; 2005.
[26] Faghri A, Zhang Y, Howell J. Advanced heat and mass transfer. Columbia, Missouri: Global Digital Press; 2010.
[27] Samara F, Groulx D, Biwole PH. Natural convection driven melting of phase change material: comparison of two methods. In: Proceedings of the 2012 COMSOL conference in Boston; 2012.
[28] Incropera FP, DeWitt DP. Fundamentals of heat and mass transfer. 5th ed. New York: John Wiley & Sons, Inc.; 2002.
[29] Zhao W, Neti S, Oztekin A. Heat transfer analysis of encapsulated phase change materials. Appl Therm Eng 2013;50:143–51.
[30] Zhao W, Elmozughi AF, Oztekin A, Neti S. Heat transfer analysis of encapsulated phase change material for thermal energy storage. Int J Heat Mass Transfer 2013;63:323–35.
[31] Mittelman G, Epstein M. A novel power block for CSP systems. Sol Energy 2010;84:1761–71.
[32] Srinivasarao P, Reddy PR, Reddy KVK. Advance power plant technologies and steam cycle for super critical application. Int J Scient Res Publications 2012;2(9).